J. Fluid Mech. (2007), *vol.* 583, *pp.* 413–422.
doi:10.1017/S0022112007006593 Printed in the United Kingdom

Saturation of inertial instability in rotating planar shear flows

R. C. KLOOSTERZIEL,[1] P. ORLANDI[2] AND G. F. CARNEVALE[3]

[1]School of Ocean & Earth Science & Technology, University of Hawaii, Honolulu, HI 96822, USA

[2]Dipartimento di Meccanica e Aeronautica, University of Rome, "La Sapienza", via Eudossiana 18, 00184 Roma, Italy

[3]Scripps Institution of Oceanography, University of California, San Diego, La Jolla, CA 92093, USA

(Received 24 January 2007 and in revised form 26 April 2007)

Inertial instability in a rotating shear flow redistributes absolute linear momentum in such a way as to neutralize the instability. In the absence of other instabilities, the final equilibrium can be predicted by a simple construction based on conservation of total momentum. Numerical simulations, invariant in the along-stream direction, suppress barotropic instability and allow only inertial instability to develop. Such simulations, at high Reynolds numbers, are used to test the theoretical prediction. Four representative examples are given: a jet, a wall-bounded jet, a mixing layer and a wall-bounded shear layer.

1. Introduction

Planar shear flows in a rotating environment are subject to both inertial and barotropic instabilities. A schematic illustrating the basic problem and geometry is shown in figure 1(*a*). The basic horizontal-shear flow $u = U(y)$ is indicated by the arrows pointing in the x-direction. The system rotates about the z-axis with angular rate $\Omega = f/2$, where f is the Coriolis parameter. Inertial instability produces perturbation vorticity aligned along the x-direction, resulting in overturning motions in the (y, z)-plane. Barotropic instability produces vorticity aligned along the z-direction resulting in meandering and possible breakup of the jet. Occurring simultaneously, these instabilities may lead to very complicated flows.

The effects of either instability acting alone can be analysed separately by imposing symmetries on the developing flow. Allowing no along-stream (x) variation would permit only the inertial instability to develop. Simulations subject to this restriction prove valuable tools in the analysis of the inertial instability. Shen & Evans (1998) and Griffiths (2003*a*) are recent studies based on this method that have revealed much about the nonlinear evolution of the inertial instability in planar shear flows. Depending on the initial velocity profile, the inertial instability may be dominant and act for a considerable time without the barotropic instability coming into play. Shen & Evans (1998) argue that this is the case for strong shear currents in the oceans' upper mixed layer. They model these currents with shear flows of high Rossby number, $Ro > 1$, where $Ro = U/fL$ with U and L being characteristic velocity and length scales. They find that the inertial instability is dominant with a growth rate at least

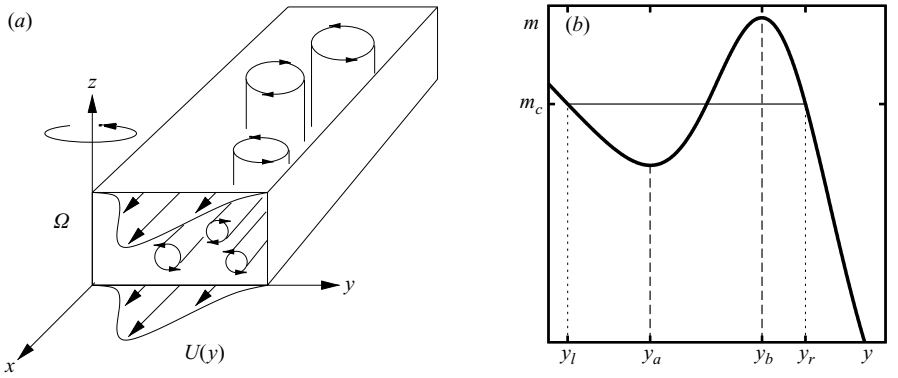

FIGURE 1. (*a*) Schematic of the rotating channel indicating the basic current $U(y)$ and two types of instabilities (inertial and barotropic). (*b*) Schematic showing how to construct the predicted momentum distribution (thin solid curve) from the initially unstable distribution (thick solid curve). The initially unstable region is $y_a < y < y_b$, that is where $\mathrm{d}m/\mathrm{d}y > 0$. Equilibration sets $m = m_c$ over the wider range $y_l < y < y_r$.

twice that of the barotropic instability. This was confirmed in fully three-dimensional simulations (Shen & Evans, 2002). Even if the initial conditions are such that the two types of instabilities grow together, or if the barotropic instability dominates, it is still interesting to understand what the effects of the inertial instability acting alone would be. It may be that this instability helps maintain the vorticity structure of the products of barotropic instability when that instability is dominant. For these reasons, it is important to understand the long-term equilibration of flows subject to inertial instability acting alone. Shen & Evans (1998), Griffiths (2003*a*) and other x-invariant studies have gone a long way toward this end. Here we present a method for predicting the final equilibrated state and test it against x-invariant numerical simulations.

The condition for inertial instability in an inviscid fluid depends on the gradient of the absolute linear momentum of the flow, $m(y) = U(y) - fy$ (Charney 1973; Holton 1992). If $f\mathrm{d}m/\mathrm{d}y > 0$, an inviscid flow is inertially unstable. This requires sufficiently strong anti-cyclonic shear, $\mathrm{d}U/\mathrm{d}y > f$. We will show that an unstable flow adjusts in such a way as to set $\mathrm{d}m/\mathrm{d}y = 0$ over a range of y that can be predicted based on a simple construction. The range over which equilibration occurs, that is where m becomes constant, is generally larger than the initial instability range. The idea for this new construction is based on a previous study of inertial instability of vortices (Kloosterziel, Carnevale & Orlandi 2007) in which we found that the range of equilibration could be determined by total angular-momentum conservation. For planar shear flows, the construction will instead be based on conservation of total linear momentum.

The construction can best be explained by considering a typical example, such as the jet-like flow shown in figure 1(*a*). The corresponding momentum distribution $m(y)$ is shown as the thick solid curve in figure 1(*b*). The vertical dashed lines indicate the instability region $y_a < y < y_b$ where $\mathrm{d}m/\mathrm{d}y > 0$. We draw a horizontal line (at level $m = m_c$) from a point on the initial profile (y_l, m_c) to the left of the instability region (see figure 1*b*), to a point (y_r, m_c) on the profile to the right of the instability region. For a simple flow with an m-distribution as in figure 1(*b*) (with a single minimum adjacent to a maximum), m_c, y_l and y_r are uniquely determined by the constraint of

total momentum conservation, i.e. by

$$\int_{y_l}^{y_r} (m_c - m(y))\mathrm{d}y = 0. \tag{1.1}$$

For $y < y_l$ and $y > y_r$ the momentum distribution remains unchanged. By construction, the predicted momentum distribution $m(y)$ has the same total momentum as the original unstable profile. In the region of constant $m = m_c$ ($y_l \leqslant y \leqslant y_r$), the predicted equilibrated velocity is $u(y) = m_c + fy$, while outside this region it is unchanged, i.e. $u(y) = U(y)$. In the examples discussed below, the values of m_c, y_l and y_r were determined with a simple search algorithm.

Another way to describe the instability condition is that fQ must be less than zero for instability, where $Q = \omega_z + f$ is the potential vorticity of the flow. In x-invariant flow, $Q = -\partial u/\partial y + f$, and setting m equal to a constant is equivalent to setting $Q = 0$. The important point is that our construction predicts the limits of the region over which $Q = 0$ in equilibrium.

2. Illustrative examples

We test the predictions of our construction against numerical simulations of the Navier–Stokes equations in four cases: a Gaussian jet, a wall-bounded jet, a mixing layer and a wall-bounded shear layer. The method of simulation is a channel model based on the staggered mesh scheme. The model is described in detail in Orlandi (2000). For the present purposes, the numerical code is modified to simulate flows invariant in the along-stream (x) direction. Thus, although there are three velocity components, they only depend spatially on the cross-stream variable y and the vertical variable z. The flow is periodic in the vertical direction, while the computational domain in the y-direction is terminated by free-slip vertical walls. Only free-slip walls are used since no-slip walls do not conserve momentum. The initial velocity field was constructed from the basic velocity field plus a random perturbation. The perturbation was applied in all three velocity components and at all points in the domain. The root mean square amplitude of the perturbation was 0.01% of max($|U|$).

Our prediction is expected to be valid for large Reynolds numbers where inertial effects dominate viscous effects. By comparison between simulations with different resolutions, we found that a resolution of 513×513 grid points would satisfactorily resolve the flow at the highest Reynolds numbers reported here. This resolution was used in all examples that follow.

2.1. *A Gaussian jet*

Our first example is the Gaussian jet

$$U(y) = U_0 \exp(-y^2/2\sigma^2), \tag{2.1}$$

where U_0 is the maximum velocity and σ the width (standard deviation) of the profile. We use these velocity and length scales to define the Reynolds number $Re = U_0\sigma/\nu$. In the following discussion, all quantities have been non-dimensionalized with the length scale σ and the time scale $1/f$. In figure 2(a), we show the evolution of the vertically averaged momentum $\bar{m}$ for the jet with $U_0 = 5$ and Reynolds number $Re = 5000$. The initial distribution is drawn as a thick dashed curve. The instability region is where the slope of this curve is positive. The predicted equilibrium profile is the thick solid curve. The thin curves represent intermediate times. Typically, there is a rapid change of the distribution as it approaches the predicted equilibrium (see the thin dashed line

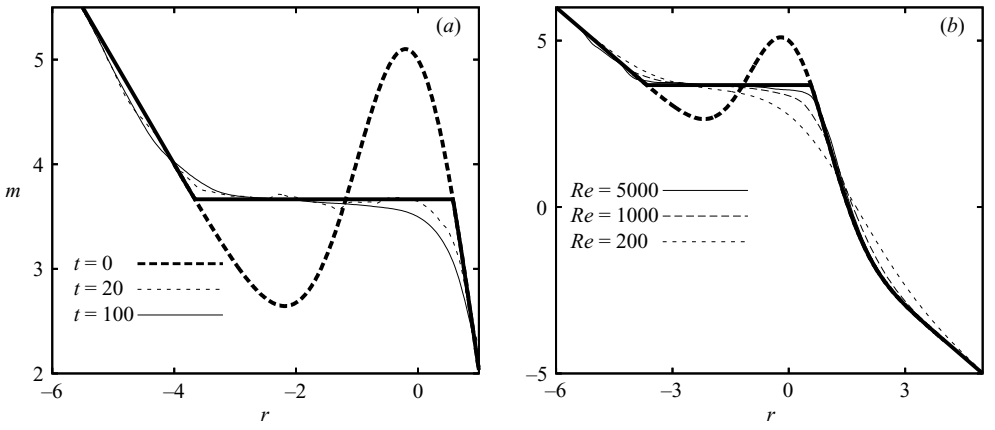

FIGURE 2. Profiles of the vertically averaged momentum m for the Gaussian jet with $U_0 = 5$. The simulation was performed on the domain $[-8 \leqslant y \leqslant 8] \times [-8 \leqslant z \leqslant 8]$ with free-slip walls at $y = -8$ and $y = +8$. (*a*) Evolution in time for the case $Re = 5000$. (*b*) Comparison at $t = 40$ of profiles with $Re = 200$, 1000 and 5000.

at $t = 20$), followed by a slow viscous-dominated diffusion of the distribution (see the thin solid line at $t = 100$).

Additional simulations were performed for a wide range of Reynolds numbers. Figure 2(*b*) shows the equilibrated profiles at $t = 40$ for $Re = 200$, 1000 and 5000. With increasing Re, the prediction is better approximated. Similar results were obtained by Griffiths (2003*a*) for zonal stratified flow on an equatorial β-plane. He showed that in a range of equilibration, for increasing Re, the final potential vorticity in his simulations approached ever closer to zero.

The process that achieves the mixing of momentum m is illustrated in the horizontal vorticity (ω_x) contour plots in figure 3(*a–c*), for the case $Re = 1000$. During the initial exponential phase of the growth of the perturbation, a vertical stack of vortices of alternating sign is formed within the inertially unstable region, that is where $\mathrm{d}m/\mathrm{d}y > 0$ (between the thick vertical dashed lines in figure 3*a*). This is just as expected from linear theory (see Ooyama 1966). These vortices represent the fastest growing perturbations, and their vertical scale decreases with increasing Re. They are overturning motions in the (y, z)-plane. As these vortices amplify in strength, nonlinear interactions result in the pairing of oppositely signed vortices, forming dipoles. The dipoles self-advect to the right or left depending on their initial orientation. They propagate outside the instability region. Mutual interactions result in a turbulent flow with dipoles moving in various directions. This is seen in figure 3*b* ($t = 14$). Note that only half of the computational domain is shown and that there are twice as many dipolar structures than are shown. We chose a moderate value $Re = 1000$ for this example in order to clearly visualize these dipoles. For much larger Re, there are far more dipoles and they are more difficult to present, unless a far smaller portion of the domain (in the vertical) is shown. Similar pairing and propagation of these vortices in the (y, z)-plane have previously been found by Griffiths (2003*b*) in a study of inertial instability on the equatorial β-plane. There is an analogous evolution in the instability of a vortex aligned along the rotation axis (Kloosterziel *et al.* 2007) where the perturbation appears as toroidal vortices encircling the initial vortex (for laboratory examples of such toroidal vortices see Afanasyev & Peltier 1998). The strongest dipole activity tends to be limited to the predicted equilibration range,

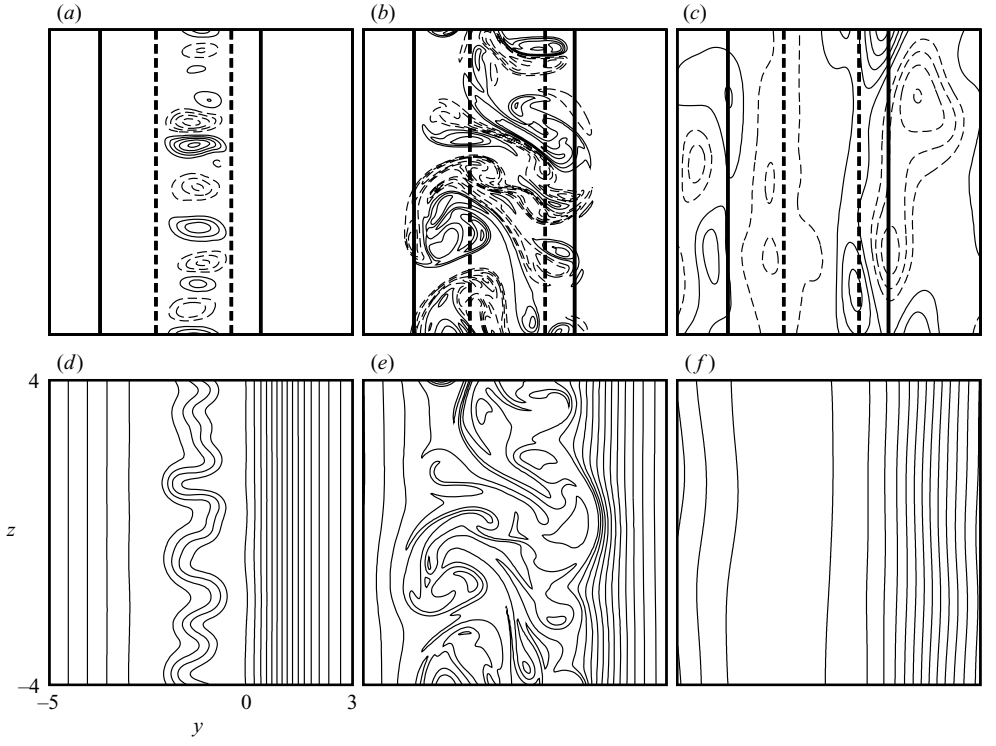

FIGURE 3. (*a–c*) The vorticity field ω_x: (*a*) $t = 10$, $\Delta\omega = 0.9$, (*b*) $t = 14$, $\Delta\omega = 1.7$, (*c*) $t = 100$, $\Delta\omega = 0.05$; solid/dashed contours represent positive/negative ω_x. The $\Delta\omega$ are the contour increments. The thick dashed vertical lines delimit the instability region. The thick solid vertical lines delimit the equilibration range. (*d–f*) The momentum field m at (*d*) $t = 10$, (*e*) $t = 14$, (*f*) $t = 100$ with contour increments $\Delta m = 0.5$. In this example $Re = 1000$. Only a part $[-5 \leqslant y \leqslant 3] \times [-4 \leqslant z \leqslant 4]$ of the full computational domain $[-8 \leqslant y \leqslant 8] \times [-8 \leqslant z \leqslant 8]$ is shown.

although there is some penetration beyond the limits of that range. At longer times, there is very low-amplitude vorticity evident everywhere (see panel (*c*) at $t = 100$), but this vorticity just continues to decay.

The corresponding evolution of the m-field is illustrated in figure 3(*d–f*). The early growth of the vortices results in the wave-like pattern in the momentum contours within the instability region (panel *d*). The effect of the dipoles in creating regions of low and high strain and generally mixing momentum is seen in panel (*e*). The effect of the dipoles penetrates well beyond the instability region, strongly affecting the whole region where change is predicted. In panel (*f*), the flow is shown at $t = 100$. At this late time, the contours of m are all nearly vertical (so that m and, hence, u has become virtually depth independent). But, a waviness that oscillates in time along these contours persists for some time. The region of well mixed m is evident.

The example shown in figure 3 is representative of moderate- and high-Re flows where nonlinear processes dominate the evolution. At lower Re, we find that, in the early stages of the evolution, the regular stack of alternating vortices still forms (as in figure 3*a*), but the vortices do not pair and translate. Instead, they decay in place, and the evolution is then dominated by viscous diffusion. The example shown in figure 2(*b*) for $Re = 200$ is such a case.

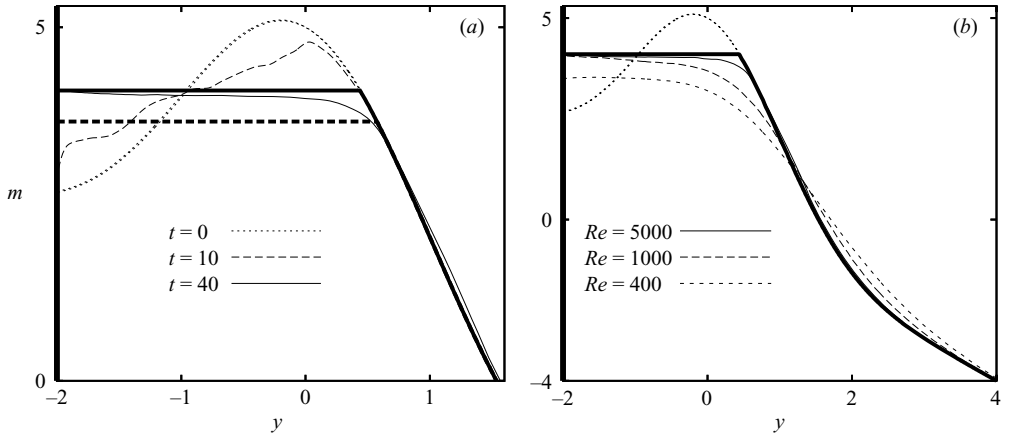

FIGURE 4. Profiles of the vertically averaged momentum m for the wall-bounded Gaussian jet with $U_0 = 5$ from the simulation on a domain $[-2 \leqslant y \leqslant 6] \times [-8 \leqslant z \leqslant 8]$. The position of the free-slip wall at $y = -2$ is indicated by a thick vertical line. (*a*) Evolution in time for the case $Re = 5000$. The predicted velocity is shown as a thick solid curve and the initial condition as a thin dotted curve. The prediction for the full mixing layer is included as a thick dashed line for comparison (compare figure 2). (*b*) m profiles at $t = 40$ for $Re = 400$, 1000 and 5000.

Viscous dissipation will eventually drain all of the energy for any finite Re. However, for the high-Re simulations discussed here, the energy loss is rapid during the inertial instability and then slow thereafter. It is the rapid adjustment phase that is of interest to us and not the slow viscous decay. Thus, it is interesting to compare the energy loss from the rapid adjustment phase with the predicted energy loss. Simple models of flows based on piecewise-linear velocity fields show that the predicted equilibrium velocity field always has less energy than the initial unstable field. We do not have a proof that our construction obeys this rule for arbitrary velocity profiles, but since these may be approximated by piecewise-linear profiles, it seems reasonable to suppose that an energy loss will always be predicted. For the $Re = 5000$ run discussed above, the predicted energy loss is 28 %, while the observed loss at $t = 40$, just after the rapid adjustment, is 23 %.

2.2. *Wall-bounded jet*

If, instead of the full jet discussed above, we consider a jet bounded by a free-slip wall, the construction for predicting the equilibrium flow may need to be modified. If the wall is inserted at $y > y_l$ where y_l is the left end of the equilibration region for the full jet, then one end of the new equilibration region will bounded by the wall. Thus we set the new y_l at the wall and follow the same procedure as before to predict the new m_c. This will be different from the full jet case, because the momentum that had been to the left of the wall is no longer available for mixing. For example, consider inserting a wall at $y = -2$ in the Gaussian jet (2.1) with the profile shown in figure 2. Since the relatively low-amplitude momentum that was redistributed from $y < -2$ in the full-jet case is no longer available, the new m_c will be larger. The construction for the wall-bounded jet is shown in figure 4(*a*). The initial jet momentum is drawn as a thin dotted line. The prediction is superimposed as a thick solid curve. The horizontal thick dashed line indicates the predicted momentum m_c for the full jet (from figure 2). As anticipated, the new level for m_c in the wall-bounded jet is higher than in the full-jet case. In terms of velocity, this change in m_c implies that the velocity in the equilibration region will be higher in the wall-bounded case than in the full-jet case.

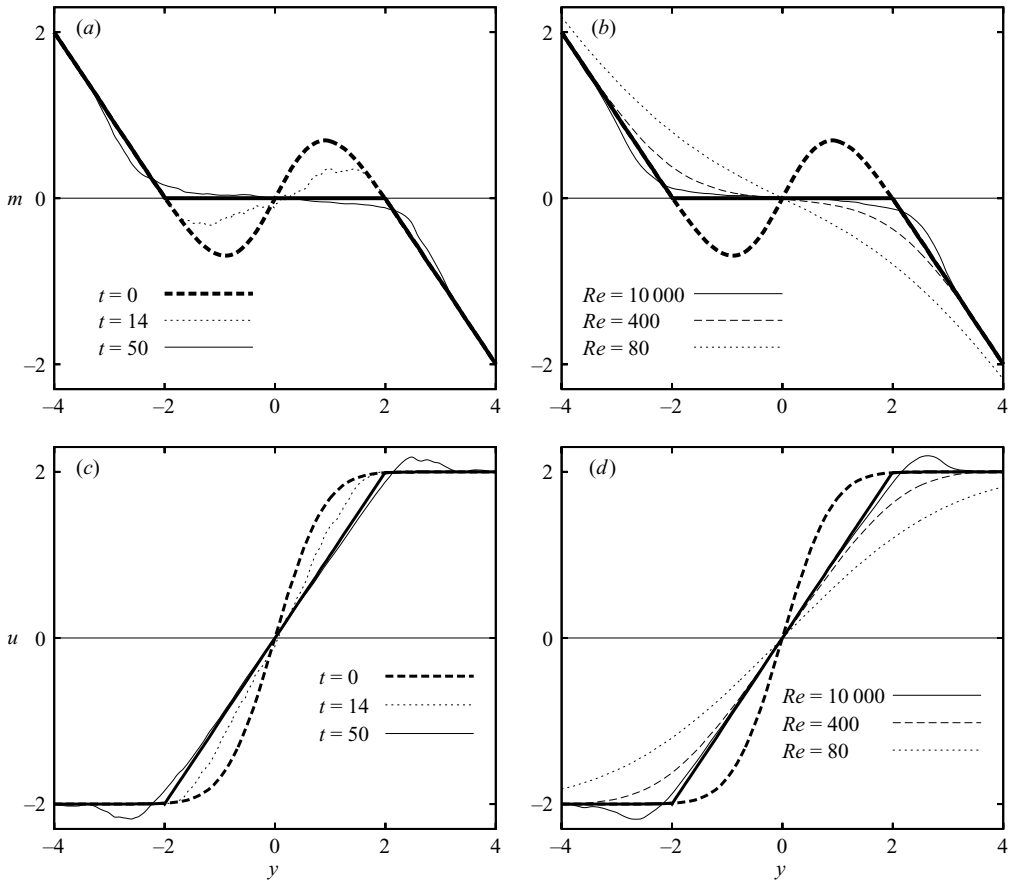

FIGURE 5. Profiles of the vertically averaged momentum m and velocity u for the mixing layer with $U_0 = 2$ from a simulation on a domain $[-16 \leqslant y \leqslant 16] \times [-16 \leqslant z \leqslant 16]$. (*a*) Evolution of m for the case $Re = 10\,000$. (*b*) Comparison of m profiles at $t = 100$ for $Re = 80$, 400 and 10 000. (*c*) Evolution of u for the case $Re = 10\,000$. (*d*) Comparison of u profiles at $t = 100$ for $Re = 80$, 400 and 10 000. In each panel, the initial profile is the thick dashed curve and the predicted profile is the thick solid curve.

Also shown is the vertically averaged momentum at times $t = 10$ and 40. Relaxation occurs very rapidly between $t = 10$ and $t = 15$. The profile at $t = 15$ (not shown) is very close to that at $t = 40$. In panel (*b*), we show the profile at $t = 40$ for different Re. This demonstrates the tendency to approach the prediction in the limit of high Re. The predicted energy loss for this case is 10 %, and by $t = 40$ the observed loss was 12 %.

2.3. *Mixing layer*

An important example of a planar shear flow, rather different from the Gaussian jet, is the horizontal mixing layer. Here there are two oppositely directed currents with a sharp velocity gradient between. A model for such a flow is

$$u = U_0 \mathrm{erf}(y/\sigma). \tag{2.2}$$

The momentum distribution for $U_0 = 2$ is shown in figure 5(*a, b*), as a thick dashed line. Although the momentum distribution is rather different from the jet case, the construction can be applied in a straightforward manner. The prediction is that,

in the equilibration range, the momentum will be mixed to $m_c = 0$. With $U_0 = 2$, the equilibration range will be $-2 < y < +2$. Beyond that range, the momentum distribution remains the same as in the initial state. The prediction is shown as a thick solid curve in panels (*a*) and (*b*). In the evolution of the vertically averaged momentum distribution, there is not much change before $t = 5$. Then the profile is rapidly transformed from the initial (thick dashed curve) toward the prediction (thick solid curve). The dotted curve in panel (*b*) shows the profile at $t = 14$, an intermediate time during this phase of the evolution. By time $t = 20$ (not shown) the profile approximates the prediction fairly well. The effect of varying the Reynolds number on the equilibrated state is illustrated in panel (*b*). For all *Re*, the equilibrated flows have $\mathrm{d}m/\mathrm{d}y \leqslant 0$ everywhere. In the equilibration region, the prediction is more closely approximated the higher the value of *Re*. However, note that there is some mismatch at the highest *Re* ($Re = 10\,000$) just beyond the equilibration region.

The evolution of the velocity profile for $Re = 10\,000$ is illustrated in figure 5(*c*). The thick dashed line shows the initial velocity profile and the thick solid line the prediction. In panel (*d*), we see that the vertically averaged velocity better approximates the prediction in the equilibration range as *Re* increases. However, for the highest *Re*, there is an overshoot just outside the equilibration range. The overshoot is related to the mismatch between the vertically averaged momentum and the prediction as seen in figure 5(*b*).

Regarding the energy balance, in this case the final predicted velocity magnitude is everywhere less than or equal to the initial value. Thus it is clear that there is a net energy loss. The percentage change will depend on how much of the domain is included in the energy calculation. Computing energy just in the region with $-4 < y < 4$ gives a predicted loss of 17 %, while the observed loss at $t = 50$ ($Re = 10\,000$) was 15 %.

2.4. *Wall-bounded shear*

Given the symmetry of the mixing layer (2.2) about $y = 0$, one might naively think that inserting a free-slip wall at $y = 0$ would not change the evolution toward the equilibrated flow on either side of the wall. However, from the point of view of momentum mixing, this cannot be, as we can see in figure 6. Negative momentum from $y < 0$ is no longer available for mixing with the positive momentum in the instability region where $\mathrm{d}m/\mathrm{d}y > 0$. Thus the predicted equilibrium m_c will have to be higher than in the full-mixing-layer case. Mixing m to a constant value $m_c > 0$ can be accomplished by mixing the momentum with $m < m_c$ at small y with higher momentum found within and just beyond the instability region. The resulting prediction, shown in figure 6 as a thick solid curve, should be compared to the full-mixing-layer prediction (thick dashed curve). The new predicted mixed region is narrower than before. The resulting predicted velocity no longer vanishes at $y = 0$ (where we put the no-slip wall). Throughout the equilibration range, the new velocity is larger than the equilibrium velocity for the positive-y side of the full mixing layer. Vertically averaged profiles for the case with $Re = 10\,000$ at $t = 13$ and $t = 20$ are also shown. In this simulation there is relatively little change in the profile before $t = 10$. Relaxation occurs very rapidly between $t = 10$ and $t = 20$. From $t = 20$ to $t = 100$, the profile does not change significantly. Again there is some overshoot compared to the prediction just beyond the end of the equilibration range. In terms of energy change, the predicted loss in the domain $0 < y < 4$ is 0.8 %, while the observed loss at $t = 20$ ($Re = 10\,000$) is 0.9 %.

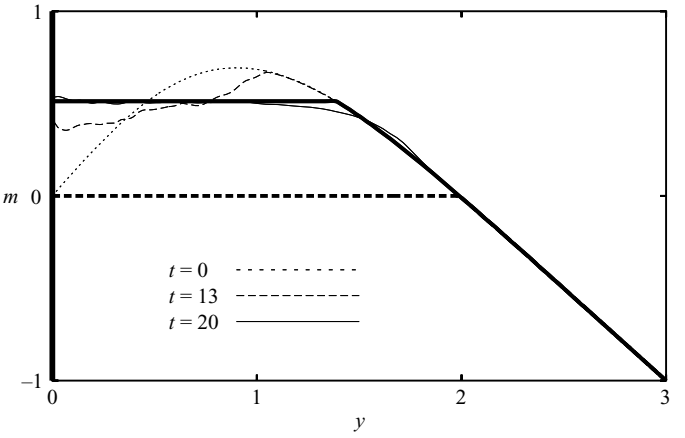

FIGURE 6. Evolution of the vertically averaged momentum m for the wall-bounded shear layer with $U_0 = 2$ from a simulation at $Re = 10\,000$ on a domain $[0 \leqslant y \leqslant 4] \times [-4 \leqslant z \leqslant 4]$. The predicted velocity is shown as a thick solid curve and the initial condition as a thin dotted curve. The prediction for the full mixing layer is included as a thick dashed line for comparison (compare figure 5). The free-slip wall at $y = 0$ is indicated by a thick vertical line.

3. Conclusion

We have introduced a simple construction that predicts the equilibrium toward which inertial instability acting alone will drive a rotating planar shear flow at large Re. The prediction is strictly valid only if the dynamics is restricted to be invariant in the along-stream direction. If this symmetry condition is relaxed, barotropic instability may compete with inertial instability. However, the present work contributes a new understanding of the tendency of the inertial instability operating in isolation. This can help analyse the competition between inertial and barotropic instabilities in the unrestricted dynamics. The construction is based on total linear momentum conservation. For simple flows, the constant value m_c to which momentum is mixed is easily determined. The prediction also gives the limits of the cross-stream range in which equilibration occurs. This is generally wider than the initial instability region. The velocity profile within this range follows from $u = m_c + fy$. Outside this range, our prediction is that the velocity profile will be unchanged. We have tested the prediction for four different types of flow and found that within the equilibration range it is approached very well as Re is increased. However, in some cases, just beyond the equilibration range, we observe a tendency to somewhat overshoot the prediction for large Re. The magnitude of the overshoot tends to increase with Re for a given time, although for a given Re it eventually decreases with time. The overshoot is caused by dipolar vortices in the (y, z)-plane which propagate somewhat beyond the predicted equilibration range. Perhaps the spikes of potential vorticity found after equilibration in the zonally symmetric simulations by Griffiths (2003*a*, figure 8) on the equatorial β-plane are analogous to these overshoots. At this point we can only speculate on the $t \to \infty$ behaviour in the $Re \to \infty$ limit. On the one hand, the construction may prove perfectly valid. On the other, although the prediction may prove valid in the predicted equilibration range, m may also be mixed to a constant value beyond that range, and then the final energy will be greater than that suggested by our construction. In fact, by mixing sufficiently far beyond the equilibration range, one can achieve a

steady state with the same energy as in the initial unstable state (at the expense of introducing discontinuities in u).

R. C. K. acknowledges support from the National Science Foundation (grants OCE 01-28991 and 05-26033), G. F. C. acknowledges support from the National Science Foundation (grants OCE 01-29301 and 05-25776), the Ministero Istruzione Universita e Ricerca (MIUR D. M. 26.01.01 n. 13) and the San Diego Supercomputer Center.

REFERENCES

Afanasyev, Y. D. & Peltier, W. R. 1998 Three-dimensional instability of anticyclonic flow in a rotating fluid: Laboratory experiments and related theoretical predictions. *Phys. Fluids* **10**, 3194–3202.

Charney, J. G. 1973 Lecture notes on planetary fluid dynamics. In *Dynamic Meteorology* (ed. P. Morel). Reidel.

Griffiths, S. D. 2003*a* The nonlinear evolution of zonally symmetric equatorial inertial instability. *J. Fluid Mech.* **474** 245–273.

Griffiths, S. D. 2003*b* Nonlinear vertical scale selection in equatorial inertial instability. *J. Atmos. Sci.* **60**, 977–990.

Holton, J. R. 1992 *An Introduction to Dynamic Meteorology*. Academic Press.

Kloosterziel, R. C., Carnevale, G. F. & Orlandi, P. 2007 Inertial instability in rotating and stratified fluids: barotropic vortices. *J. Fluid Mech.* **583**, 379–412.

Ooyama, K. 1966 On the stability of the baroclinic circular vortex: a sufficient condition for instability. *J. Atmos. Sci.* **23**, 43–53.

Orlandi, P. 2000 *Fluid Flow Phenomena: A Numerical Toolkit*. Kluwer.

Shen, C. Y. & Evans, T. E. 1998 Inertial instability of large Rossby number horizontal shear flows in a thin homogeneous layer. *Dyn. Atmos. Oceans* **26**, 185–208.

Shen, C. Y. & Evans, T. E. 2002 Inertial instability and sea spirals. *Geophys. Res. Lett.* **29**, 21–24.